





Searching for a Signature of Turnaround in Galaxy Clusters with Convolutional Neural Networks

Nikolaos Triantafyllou^{1,2,3} , Giorgos Korkidis^{1,2} , Vasiliki Pavlidou^{1,2} , and Paolo Bonfini¹ 

¹ Department of Physics and Institute for Computational and Theoretical Physics, University of Crete, 70013 Heraklio, Greece
e-mail: : gkorkidis@physics.uoc.gr

² Institute of Astrophysics, Foundation for Research and Technology – Hellas, Vassilika Vouton, 70013 Heraklio, Greece

³ Scuola Normale Superiore, Piazza dei Cavalieri 7, 56126 Pisa (PI), Italy
e-mail: : nikolaos.triantafyllou@sns.it

ABSTRACT

Context. Galaxy clusters are important cosmological probes that have helped to establish the Λ CDM paradigm as the standard model of cosmology. However, recent tensions between different types of high-accuracy data highlight the need for novel probes of the cosmological parameters. Such a probe is the turnaround density: the mass density on the scale where galaxies around a cluster join the Hubble flow.

Aims. To measure the turnaround density, one must locate the distance from the cluster center where turnaround occurs. Earlier work has shown that a turnaround radius can be readily identified in simulations by analyzing the 3D dark matter velocity field. However, measurements using realistic data face challenges due to projection effects. This study aims to assess the feasibility of measuring the turnaround radius using machine learning techniques applied to simulated observations of galaxy clusters.

Methods. We employ N-body simulations across various cosmologies to generate galaxy cluster projections. Utilizing Convolutional Neural Networks (CNNs), we assess the predictability of the turnaround radius based on galaxy line-of-sight velocity, number density, and mass profiles.

Results. We find a strong correlation between the turnaround radius and the central mass of a galaxy cluster, rendering the mass distribution outside the virial radius of little relevance to the model’s predictive power. The velocity dispersion among galaxies also contributes valuable information concerning the turnaround radius. Importantly, the accuracy of a line-of-sight velocity model remains robust even when the data within the R_{200} of the central overdensity are absent.

Key words. large-scale structure of Universe – methods: data analysis – methods: numerical – galaxies: clusters: general

1. Introduction

Observations of the large scale structure in the Universe validate the Λ CDM model, with the exception of some apparent contradictions, referred to as “tensions”, particularly in relation to observations of the Hubble parameter and σ_8 (see e.g., Bernal et al. 2016; Zhao et al. 2017; Joudaki et al. 2017; Hildebrandt et al. 2017; Riess et al. 2018, 2019; Motloch & Hu 2018; Planck Collaboration et al. 2020; Raveri & Hu 2019; Adhikari & Huterer 2019; Handley 2021; Di Valentino et al. 2020, 2021; Shah et al. 2021). Current observational evidence for the existence of a cosmological constant is based on the relation between the present-day values of the cosmological density parameters of matter, Ω_m and dark energy, Ω_Λ , probed either by the cosmic microwave background or by observations of distant supernovae. Other cosmological datasets (cluster abundances, baryon acoustic oscillations) are also sensitive to Ω_m , but much less so to Ω_Λ . Recent work (Pavlidou et al. 2020; Pavlidou & Tomaras 2014; Korkidis et al. 2020, 2023; Tanoglidis et al. 2015, 2016) has demonstrated that the turnaround density (ρ_{ta}) can be used to impose novel constraints on the cosmological parameters, highlighting that all structures share the same ρ_{ta} for the same redshift and cosmology.

The turnaround scale (also known as the turnaround radius, R_{ta}) marks the boundary where matter surrounding a collapsed cosmic structure transitions, on average, into the Hubble flow

(Korkidis et al. 2020). Turnaround is not a singular event in a structure’s history. Instead, it is a continuous phenomenon observable around all structures at any given time. For example, around a big galaxy cluster, there is a region where material is actively accreting. However, beyond a certain distance, the expansion of the universe sweeps away other structures. The intersection of this accretion region with the Hubble flow occurs at the scale often referred to as the zero-velocity shell, the turnaround radius.

To accurately determine ρ_{ta} , it is essential to have knowledge of both R_{ta} and M_{ta} (the mass enclosed inside the turnaround radius). For very nearby objects it may be possible to reconstruct the turnaround mass and radius from the peculiar velocity field (e.g., Hoffman et al. 2018). However, in general, these methods do not scale with distance. The primary observational data that are widely available even for distant clusters are the distribution of galaxies as seen on the plane of the sky and their line of sight velocities. This limitation means that the turnaround radius cannot be reliably calculated by analyzing the velocity profiles directly; at a turnaround radius away from the center of the cluster as seen on the plane of the sky, the velocity component that transitions from positive to negative at turnaround is entirely on the plane of the sky, hence not observable. For the measurement to occur along the line of sight, distances of individual galaxies need to be measurable independently of their redshifts, and these are available only for nearby clusters. Consequently, researchers

must rely on indirect methods or theoretical models to estimate the turnaround radius, such as the use of Zel’dovich sheets, as explored in Lee et al. (2015); Lee & Yepes (2016); Lee (2016); Lee & Li (2017); Lee (2018). Here, we explore a different approach, and test the feasibility of using machine learning tools directly on (simulated) galaxy position, mass and line-of-sight velocity data to identify the turnaround radius of a galaxy cluster.

The use of machine learning methods, and in particular the subcategory of deep learning algorithms, i.e. Artificial Neural Networks (NNs), has experienced an exponential growth in astrophysical and cosmological studies over the recent years (Lahav 2023; Baron 2019; Carleo et al. 2019; Huertas-Company & Lanusse 2023), with several discussions on the effectiveness of these data driven methods (Lin et al. 2022). As per the universal approximation theorem, NNs—essentially compositions of weighted sums—are universal function approximators, capable of representing any continuous function in the limit of infinite parameters. Consequently, they serve as powerful tools for exploring data, with feature extraction capabilities embedded in their internal structure. For this reason, we adopt such an approach to investigate which types of observational datasets may encode information on the R_{ta} of galaxy clusters.

In particular, we wish to establish whether there exists, *in principle*, a way of measuring the turnaround radius on the plane of the sky, using information on the distribution of galaxies around galaxy clusters, their masses, and their line-of-sight velocities. To this end, we employed N-body dark matter simulations to create projections of dark matter halo clusters (since baryonic effects are negligible at these scales, we use the terms “halo” and “galaxy” interchangeably) and measured their turnaround radii from their velocity profiles. We then applied machine learning techniques to establish a relationship between these projections and the accurate, numerically computed turnaround radii derived from the 3D information on the dark matter distribution and velocity field available in the simulations.

The outline of this paper is as follows: In Sect. 2 we describe the set of N-body simulations used in this work and the characteristics of the resulting turnaround radii. In Sect. 3 we describe the methods used for the creation of the model that tries to predict the turnaround radius and in Sect. 4 we present the results of our analysis. We discuss these findings in Sect. 5.

2. Data

2.1. N-body Simulations

In this work we use data from: (a) The MultiDark Planck 2 (MDPL2) Simulation (Riebe et al. 2013). The MDPL2 simulation was performed with $(1\text{Gpc}/h)^3$ box size, with about 57 billion particles and a cosmology consistent with Planck Collaboration et al. (2014). It was performed using the L-Gadget2 code. (b) The Virgo Intermediate Scale Simulations simulations (Λ CDM, OCDM, SCDM) (Frenk et al. 2000; Thomas et al. 1998; Jenkins et al. 1998). These simulations contain 256^3 particles each in a box of $(239.5\text{Mpc}/h)^3$ and represent different cosmological models. The calculations were done using the external AP3M N-body code. For a more in depth description of the simulated boxes and the halo sample selection the reader is referred to Korkidis et al. 2023. For reference we include in Table 1 the main parameters of the 4 simulated boxes.

Similarly, we used the same cluster sample as in Korkidis et al. 2023 for the purposes of generating our mock cluster catalog, consisting of the largest ~ 3200 and ~ 1000 halos of the MDPL2 and Virgo simulations respectively. For each cluster in

this sample, we calculated the turnaround radius kinematically by measuring the mean velocity of dark matter particles in spherical shells as described by Korkidis et al. (2020). The distribution of the turnaround radii values for the MDPL2 and Virgo Λ CDM simulations at $z = 0$, along with some 1-point statistics, can be seen in Fig. 1.

2.2. Mock projections of Galaxy Clusters

Next, we projected all galaxy-sized halos ($M_{200} \geq 10^{12}M_{\odot}$) around each cluster, onto each of the cluster’s three principal planes, retaining information on their positions and velocities perpendicular to the planes. These velocities would be equivalent to the line-of-sight velocities as observed by an observer situated far from the cluster. Employing three projections augmented our sample size by a factor of three, a crucial benefit for the effective training of our model. The projected area for each plane was chosen to be a square region of 25 Mpc on each side, centered on the respective cluster. This dimension was selected to ensure it would encompass the largest turnaround radius identified in our sample.

Lastly, the projection depth for the galaxies was informed by the varying uncertainties associated with different types of galaxy redshift surveys, specifically those employing either photometric or spectroscopic redshift measurements. Consequently, we created two distinct projected samples to reflect these different levels of redshift accuracy. In practical terms, this led to the imposition of a velocity cut on the velocities perpendicular to the projection plane, set at approximately 10^3km/s , and 10^4km/s , for spectroscopic and photometric redshift surveys, respectively.

All of the aforementioned steps were carried out at $z = 0$. For the MDPL2 (Virgo Λ CDM) data we additionally considered another 2 redshift snapshots, namely $z = 0.49$ and $z = 1.03$ ($z = 0.5$ and $z = 1.0$). In the histograms of Fig. A.1 we can see the distribution of the R_{ta} values from each of the additional MDPL2 redshift snapshots (left panel) and from each of the non- Λ CDM Virgo simulations at $z = 0$ (right panel). The different location of peaks in different redshifts and different cosmologies is a direct indication that ρ_{ta} is a function of redshift and cosmological parameters.

3. Methods

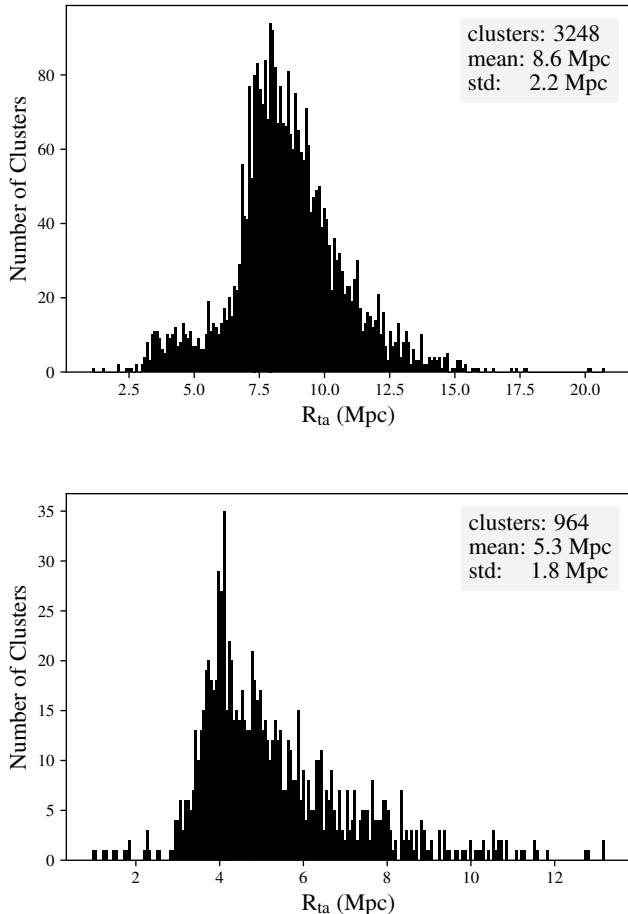
3.1. Post-processing

As mentioned in Sect. 2, our data consists of projected regions around cluster-sized dark matter halos, incorporating the details of each halo’s coordinates, virial mass and line-of-sight velocity. This format is not suitable for our analysis. Hence, in order to feed the data to the algorithm we converted them into images as 2D histograms. For the histograms we used appropriate weights to create 3 types of images: mass column density, number column density and mean line-of-sight velocity in each bin, in our case. We have not considered observational errors in each “observed” quantity. The reason for not adding noise is that we want to provide the model with the most favorable conditions possible. Should our present analysis fail to identify the turnaround scale, it is then certain that it will also fail in noisy datasets. However, if we succeed in identifying the turnaround scale, clearly further analysis will be needed to quantify the effect of noise, before proceeding to the analysis of real data.

For the first two cases (mass column density and number column density), the transformation does not change the nature of the data since we are merely normalizing by dividing by the area

Table 1. Simulation box size in h^{-1} Mpc, number of particles, particle mass in $h^{-1}M_{\odot}$, Force resolution in units h^{-1} kpc and cosmological parameters. All simulations are from dark-matter-only runs.

Simulation	Box	Particles	M_p	Ω_m	Ω_b	Ω_{Λ}	h_{100}
MDPL2	1000	3840^3	1.51×10^9	0.307115	0.048206	0.692885	0.6777
Virgo Λ CDM	239.5	256^3	6.86×10^{10}	0.3	-	0.7	0.70
Virgo SCDM	239.5	256^3	22.7×10^{10}	1.0	-	0.0	0.50
Virgo OCDM	239.5	256^3	6.86×10^{10}	0.3	-	0.0	0.70


Fig. 1. Histogram of the turnaround radii R_{ta} values from MDPL2 (*upper panel*) and Virgo Λ CDM (*bottom panel*). The difference between the two distributions reflects the difference between box sizes and resolutions.

of each pixel (constant) to acquire the densities. For example for the mass column density we have:

$$\{\text{pixel}_i\} = \sum_{h \in \text{halos in } i} \frac{M_h}{\text{pixel area}}. \quad (1)$$

For the third case, by taking the mean velocity, some of the pixel values may change relative to one another in comparison with just binning the velocities, since we are dividing each pixel with a different number of halos, i.e

$$\{\text{pixel}_i\} = \frac{1}{N_i} \sum_{h \in \text{halos in } i} \frac{v_{\text{los},h}}{\text{pixel area}} \neq \sum_{h \in \text{halos in } i} \frac{v_{\text{los},h}}{\text{pixel area}}, \quad (2)$$

where N_i the number of halos in pixel i . However, we discovered through several tests that this contributes positively to the outcome of our model. In addition to the original 3 types of images we also considered a 4th type: the velocity dispersion in each bin, as a more promising (in terms of NN performance) and realistically observed quantity.

Different resolutions of the images were tested; we chose 25×25 pixel images as optimal, both in terms of accuracy and computational efficiency. Higher resolution images have too many zero-valued pixels which appears to confuse the algorithm. Changes in the network's structure with the use of 11 and 12 regularizations, which constrain the synaptic weights of the network, were not found to increase the high-resolution model's performance. Similarly, changes in the nature of the projected images by scaling the data (min-max scaling, standardization) or by exchanging the 0-valued pixels with the mean or the median of the training set, produced unsatisfactory results. The issue was mitigated solely by the resolution choice.

We can see from Fig. 1 that the turnaround radius data are not uniform but rather they present a Gaussian distribution-like form (descending towards the right side due to the halo mass function and towards the left due to our sampling). This could potentially result in the algorithm only predicting values close to the peak, resulting in a problem usually referred to as mode collapse (Lin et al. 2022). We tried to transform the R_{ta} data so that the distribution of the values is less likely to affect the model. Namely we tried to pass R_{ta} through an invertible function to transform the data into a uniform distribution. The results showed that the original data were more successful and our final models are not affected by this issue.

Commonly, for each case, 80% of the simulation data were used for the training and validation and 20% were used for testing the trained model.

3.2. Convolutional Neural Networks

In the introduction of this paper, we established the potential of NNs for predicting R_{ta} , we now focus on designing a model specifically tailored to the nature of our data. The observational proxies for R_{ta} are inherently spatial in nature, represented as 2D projections of galaxy distributions, along with their masses and their velocities.

This spatial structure necessitates a NN architecture capable of effectively capturing and analyzing such features. In conventional NNs, the layers are fully connected, designed primarily for one-dimensional inputs. In this work, we use Convolutional Neural Networks (CNNs), which are best suited for single and multi-channel images (2D and 3D inputs). CNNs use convolutional layers which connect the neurons of one layer only to a small region of the neurons of the previous layer (e.g. pixels of the image), allowing for the recognition of low level spatial features. The main structure of our NN can be seen in Table B.1.

This structure was the best candidate in almost all of the trials performed as it was favored by our optimization study.

3.3. Metrics

To evaluate the accuracy of the predicted R_{ta} , we utilized established statistical metrics: the coefficient of determination (R^2 score) and Shapley values.

We use the R^2 score to evaluate the accuracy of the model, by comparing the predicted and the true R_{ta} . An R^2 score of 1.0 signifies that the model accurately predicts the target variable (R_{ta}) based on the feature variables (projections). Conversely, an R^2 score of 0 indicates that the model does not predict the target variable at all, i.e., the model is no better than simply taking the mean of the target variable distribution. Notably, the R^2 score can become negative when the chosen model fits the data worse than a horizontal hyperplane.

In the context of machine learning, and the interpretability of its models, Shapley values provide a method to allocate the contribution of each feature to the prediction for each individual instance. The Shapley value of a feature can be interpreted as its average marginal contribution to the prediction, across all possible combinations of features.

4. Results

In this section, we detail the outcomes of our analysis. Our primary focus is assessing the predictive capability of our trained CNN in determining the R_{ta} of simulated clusters, utilizing their various mock projection images. We specifically examine the network’s effectiveness, trained on different mock data, including the mass distribution of galaxies proximal to the clusters, as well as their velocity distribution, the surrounding galactic number density, and varying levels of halo projection around the clusters as viewed in the plane of the sky (initially the 3 types of histograms of Sect. 3.1 with the 2 velocity cuts, while considering the 4th type in Sect. 4.3). Additionally, we consider the impact of the central cluster region data on our model and, we evaluate the model’s predictive accuracy when tested in a cosmological setting different from the one in which it is trained.

4.1. General

Initially, we focused on analyzing projected cluster images from the MDPL2 simulation at redshift $z = 0$, applying both low and high velocity cuts to get a general idea of the potential of our methodologies. As outlined in Sect. 3.2, CNNs can be utilized with both single and multi-channel inputs, enabling us to merge our 3 types of post-processed single-channel mock data images (mass column density, number column density, mean line-of-sight velocity) in various configurations to generate multi-channel images. For instance, combining all three data types can be thought of as an RGB image, with the R, G, and B channels representing our distinct data types.

The outcomes of training the network with all possible data combinations are illustrated in the upper panel of Fig. 2, depicted as a histogram of the R^2 scores derived from the test set for each combination, displayed along the x-axis. Training with the low velocity cut data yielded the highest accuracy, as evidenced by the superior R^2 scores marked by blue bars. This result was anticipated, given the increased projection depth contamination associated with the high velocity cut.

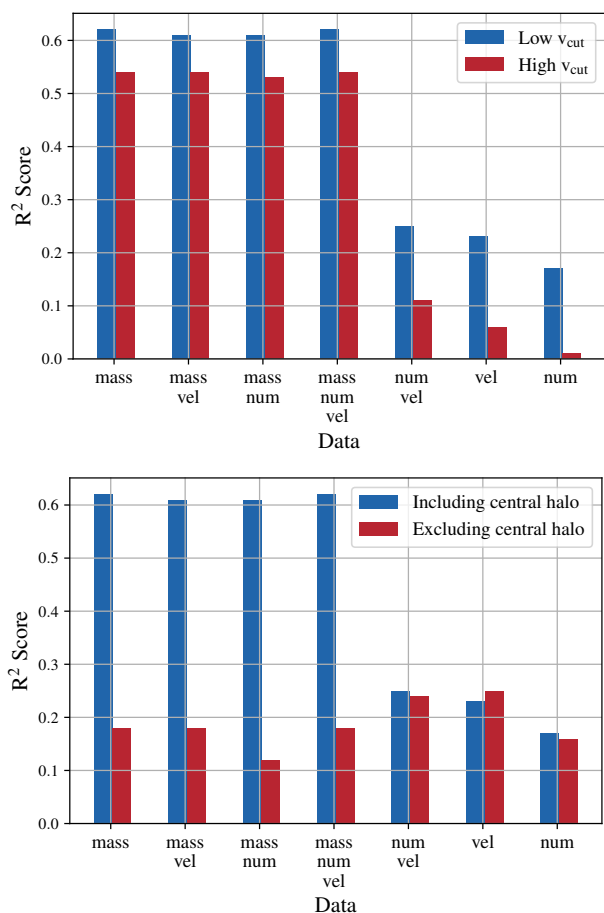


Fig. 2. Performance comparison across different models. *Upper panel:* Comparison between low- and high- velocity-cut models performance. The plot shows different R^2 values for each combination of the 3 features considered: mass column density, number column density and mean line-of-sight velocity (indicated as “mass”, “num”, and “vel” respectively). Best results are obtained for the low velocity cut (due to less contamination) and for data containing the mass. *Lower panel:* Comparison between models including or excluding the central halo. Both analyses are performed for the low-velocity-cut data. Without the central halo, performance drops significantly across models; all models without it predict the turnaround with similar score.

Models incorporating mass column density images demonstrated the highest accuracy, as indicated by the first four bar pairs, aligning with expectations that the gravitational influence of a cluster’s mass correlates with the distance from the cluster’s center where the Hubble flow becomes dominant. Mean velocity data did not exhibit a strong correlation with the R_{ta} . We aim to delve deeper into these observations in Sects. 4.2 and 4.3, examining the cases of mass column density and velocity in further detail. Moving forward, we will exclusively consider the low-velocity-cut data, corresponding to the high-accuracy-redshift case, aiming to examine the most favorable scenario possible.

4.2. Mass distribution

In the previous section, a significantly better performance of the models trained on data containing the mass was established. This leads us to investigate what the model’s performance would be without information on the central, more massive halo (i.e. without information on the mass of the central collapsed galaxy cluster).

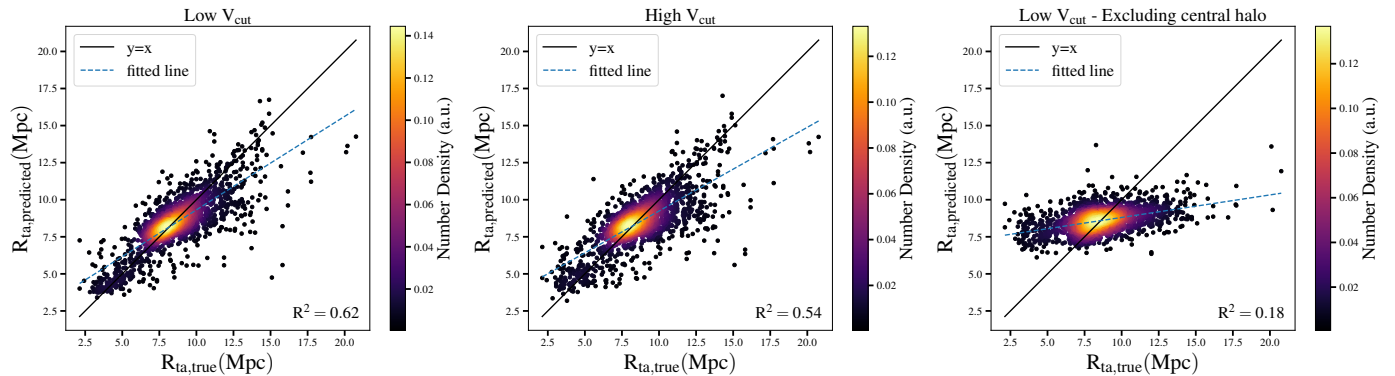


Fig. 3. Comparison between predicted and true values of R_{ta} for different CNN models, when using mass information. The colors represent the number density of the plotted points, calculated using a Gaussian kernel density estimate. While the models in the left and middle panel show some correlation between true predicted R_{ta} values, the right-panel model appears to mostly predict the mean value of the R_{ta} distribution.

To this end, we removed the central halo completely from all of the regions and re-trained our model with the low-velocity-cut data from the MDPL2 $z = 0$ output. The results can be seen in the lower panel of Fig. 2. Without the central halo, the performance of the mass-containing models drop significantly: there is a very noticeable difference between the height of the blue and red bars in the first 4 models. This implies that their better performance was due to the information contained in the central halo’s mass. All of the other models predict the turnaround with about the same score.

A more accurate representation of these results is shown in Fig. 3 with scatter plots between the predicted values of the turnaround radii and their real values. If the model was perfect then all the points $(R_{ta,predicted}, R_{ta,true})$ would be located on the $y = x$ (black solid) line. In the case where the central halo is missing (right panel) there seems to be a little to no correlation whatsoever. This result underscores that what the model is extracting and learning in the first two cases (left and middle panel) is a correlation between the central mass and the turnaround radius (which has been shown to exist analytically, Korkidis & Pavlidou 2024) rather than some actual image feature at the location of the turnaround radius itself.

We also evaluated our model in cosmological settings different than the one our model was trained. The R^2 score from different redshifts from MDPL2 and from different cosmologies from both MDPL2 and the Virgo Simulations can be seen in the upper panel of Fig. 4 (left and right panel respectively) where larger circles correspond to higher R^2 scores. Best models seem to be the ones trained with the data from MDPL2, most likely due to the larger training dataset. Additionally, a model trained at one redshift is not successful when tested at a different one. Models perform worse as the redshift of the test set moves further away from the redshift of the training set, as indicated by the decreasing size of the circles as we move away from the diagonal in the upper left panel of Fig. 4. If we accept that the model is primarily reconstructing the scaling of the central massive halo with the turnaround radius, this behavior is expected because of the redshift dependence of ρ_{ta} , and of its scaling with the central halo mass.

4.3. Velocity distribution

In Sect. 4.1, we observed that velocity data alone did not yield significant information. A model trained and tested solely on velocity data performed unsatisfactorily. Given the known correlation between the mass of the central halo and R_{ta} , and also

between velocity dispersion and mass of the central halo, one would rather anticipate a correlation between the velocity dispersion of surrounding halos and the central halo’s mass, and consequently, the turnaround radius. To address this, we explore a 4th type of data: the velocity dispersion.

4.3.1. Stacking

Our initial focus was on the MDPL2 data at $z = 0$. We hypothesized that the sparsity of galaxies in computing a velocity dispersion image might obscure any relationship with the R_{ta} . To counteract this, we employed a “stacking” technique for our projections, based on their respective R_{ta} values. This stacking involved categorizing the R_{ta} into bins and merging data from clusters within the same bin. We then assigned a new R_{ta} value for each bin, calculated as the mean of the R_{ta} values within it. The motivation here is that clusters normalized with respect to overdensity radii or masses are known to exhibit similar dynamical characteristics. Subsequently, as detailed in Sect. 3.1, we transformed these data into images. This time, however, we focused on computing the standard deviation of the velocities within each bin.

After incorporating the new data type into our training process, we reassessed the model’s performance on the test set. The left panel of Fig. 5 displays the comparison between the true values and those predicted by the model, which was trained using 3000 R_{ta} bins. This approach yielded approximately 1200 cluster images, as some bins were devoid of data. Our analysis revealed a modest improvement in correlation, as evidenced by the increase in the correlation coefficient (from $R^2 = 0.24$ to $R^2 = 0.36$, comparing with the one of Fig. 2). Although this enhancement in correlation is not markedly significant, it suggests that a stacking approach, based on variables influencing cluster dynamics, holds promise for future research applications.¹

4.3.2. Merging

From the left panel of Fig. 5 we realized that the model is subject to the problem of mode collapse, where it just tends to predict values close to the mean of the parent distribution. To address the issue, we merged data from the MDPL2 and Virgo Λ CDM ($z = 0$) simulations. Despite slight differences in simulation parameters, the turnaround radius should theoretically be ascertain-

¹ The results of a similar approach but by stacking images based on their R_{200} can be found in Fig. D.1 of the appendix.

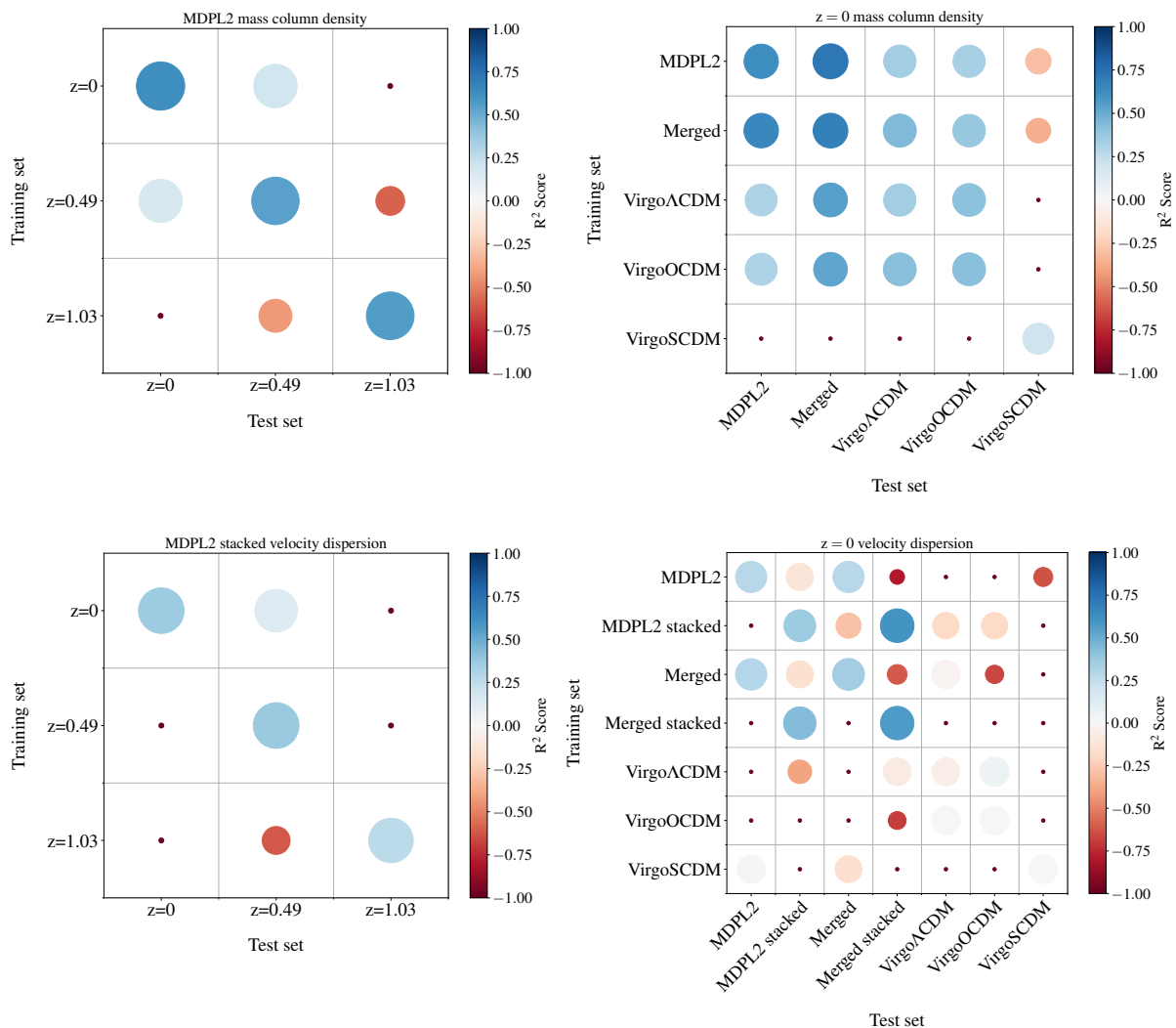


Fig. 4. R^2 scores of different combinations of training and testing data using the mass column density (*upper panel*) or velocity dispersion (*lower panel*) information (size of circles indicates $|R^2|$ for easier comprehension of general trends). 80% of the simulation data were used for training-validation and 20% was used for the testing in each case located in the diagonal. *Left panel:* Training and testing data from different MDPL2 redshifts ($z=0, 0.49, 1.03$). As expected, for each training set the R^2 score is the highest when evaluated on data from the same redshift. Since MDPL2 is a Λ CDM concordance cosmological simulation, the ρ_{ta} depends on redshift. Therefore, for different redshifts the model cannot find an apparent correlation between M_{vir} and R_{ta} because ρ_{ta} varies with redshift. The velocity information plot has the same form as the mass, indicating that the model just correlates the mass with the velocity dispersion. *Right panel:* Training and testing data from different simulations and cosmological models (MDPL2, Virgo Λ CDM, Virgo OCDM, Virgo SCDM and the merged data from MDPL2 and Virgo Λ CDM). Best models seem to be the ones containing the data from the MDPL2 possibly due to the fact of the larger number of training instances.

able regardless of these minor variances. The outcomes of this merged data analysis are presented in the middle panel of Fig. 5. The achieved R^2 Score of 0.57, coupled with the graphical comparison of predicted versus true values, strongly suggests a significant correlation.

For additional context, we have analyzed various stacked images by categorizing the R_{ta} values into nine distinct bins. These are illustrated in Fig. C.1. It is important to highlight that identifying the R_{ta} values based solely on these images poses a challenge. This difficulty is especially pronounced for values that fall outside the R_{ta} range of 4.3 – 10.6 Mpc.

4.3.3. Interpretability and information inside R_{200}

To better understand our findings, we analyzed the Shapley values of the pixels in a selection of test images, as depicted in Fig. 6. Our observations reveal a notable trend: a higher stan-

dard deviation in velocity in areas around the center tends to lead the algorithm to predict a lower R_{ta} value, and conversely, a lower velocity standard deviation suggests a higher predicted R_{ta} . This pattern appears to support our initial hypothesis of a correlation between velocity dispersion and the mass of the central halo. However, it is crucial to note that these conclusions are drawn from just two specific examples. While Shapley values offer valuable insights, they are indicative rather than definitive. Nevertheless, a common pattern observed across most of the analyzed test images is the algorithm's apparent emphasis on the central region of the cluster in making its predictions.

To further explore the CNN model's apparent focus on the central region of structures, we conducted an experiment by removing all halos within the R_{200} radius of each cluster's central overdensity, followed by retraining the model. The performance of this modified model is illustrated in the right panel of Fig. 5, where it achieved an R^2 score of 0.59, comparable to previous

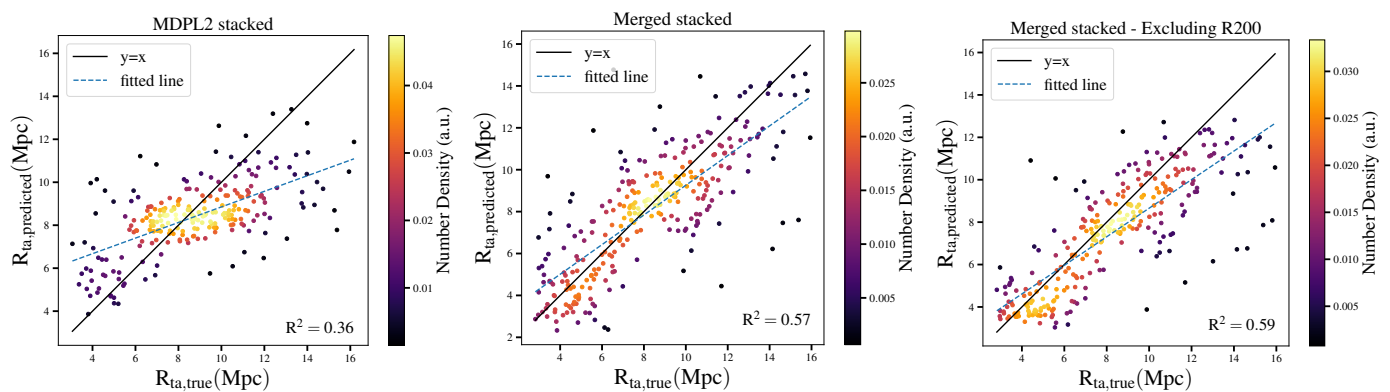


Fig. 5. Comparison between predicted and true values of the R_{ta} for models using the “stacked” images from 3000 bins of R_{ta} from: the MDPL2 data (*left panel*); the merged MDPL2 with Virgo Λ CDM data (*middle panel*); the merged MDPL2 with Virgo Λ CDM data with removed information inside the R_{200} of the central overdensity (*right panel*). R^2 scores are 0.36, 0.57 and 0.59 respectively. The colors represent the number density of the plotted points, calculated using a Gaussian kernel density estimate. It is apparent that the merging of the 2 datasets significantly improves the performance of the model even without the central halos’ velocity information.

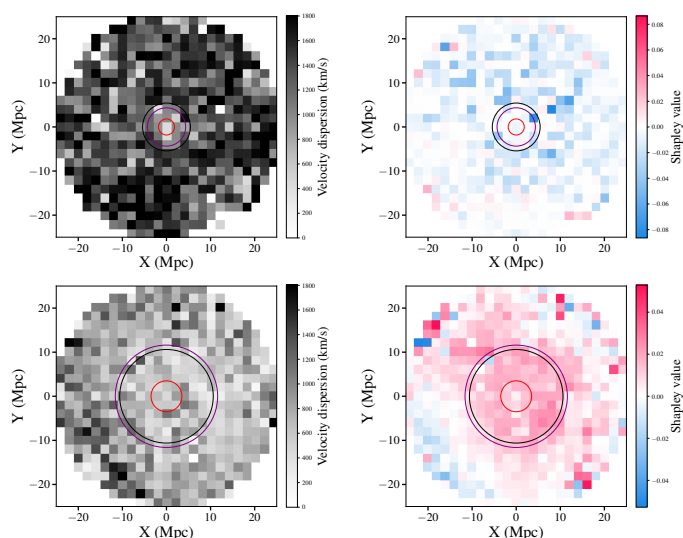


Fig. 6. Shapley values of 2 random test projections (*upper and lower panel*) from the merged and stacked MDPL2 and Virgo Λ CDM data. *Left panel*: Standard deviation of the halo velocity in each pixel. *Right panel*: Shapley values in each pixel (pink: higher prediction; blue: lower prediction). The red circle represents the R_{200} , while the black and purple circles represent the true and the predicted R_{ta} respectively. Lower dispersion is always prominent in the central area due to the virialization of the matter surrounding the central perturbation. However, the extent of this lower dispersion area seems to indicate to the model where the turnaround radius should be. In particular, in the first image, the structure seems to have higher dispersion in areas far from the center, compared to the second one which has lower values. The high dispersion seems to indicate to the model that the turnaround radius should be lower while the lower dispersion indicates the opposite.

results. This outcome suggests that the information within the R_{200} of the central overdensity is not critically important for the model’s predictions when analyzing velocity dispersions.

In a methodology parallel to that described in Sect. 4.2, we conducted several training iterations with varying combinations of training and test sets across different cosmological scenarios. The R^2 scores obtained from these experiments, involving different redshifts from MDPL2 and diverse cosmologies from both MDPL2 and the Virgo Simulations, are presented in the

lower panel of Fig. 4 (left and right panels, respectively). Models trained with MDPL2 data consistently showed better performance, likely due to the more extensive training dataset. The R^2 scores across different redshifts mirrored the patterns observed in the upper panel of Fig. 4, which were based on the CNN trained with mass data: models trained in one specific cosmology did not predict accurately when tested in another. These results collectively suggest that the velocity dispersion information used by the CNN to predict R_{ta} correlates with the mass of the central overdensity. Consequently, similar to the limitations observed with mass data, the model struggles to accurately predict R_{ta} across different redshifts and cosmologies.

5. Conclusions

The turnaround density of galaxy clusters has been established as a novel cosmological probe and a means to further test the current cosmological model (Pavlidou & Tomaras 2014; Pavlidou et al. 2020; Korkidis et al. 2020, 2023). In this work, we explore a method to estimate the turnaround radius of galaxy clusters based on their projected distributions on the plane of the sky. Using cosmological N-body simulations, we generate idealized observational data—incorporating mass and velocity information without uncertainties—within two “slices” of varying thicknesses, corresponding to what is achievable in spectroscopic and photometric surveys. The “true” turnaround radii are derived from the velocity profiles surrounding the central overdensities of galaxy clusters in the simulations. Then, a Convolutional Neural Network (CNN) is trained to predict the turnaround radius, utilizing various combinations of training and test data from different simulations, redshifts, and cosmologies.

When the model is trained on individual clusters we find that the mass is the most important information we have for the prediction of the turnaround radius. This at first may appear counter-intuitive as the turnaround is defined and computed by the velocity profiles of the dark matter particles around the central halo. However, it is the mass of the cluster that contributes to the gravitational dynamics defining the turnaround radius. Furthermore, we find that the mass of the central, more massive halo, is almost entirely contributing to this prediction. In the context of the findings of Korkidis & Pavlidou (2024), this is not surprising: R_{ta} is an overdensity radius, so its value is entirely determined at a given redshift and for a given cosmology by the enclosed mass;

and that enclosed mass has been shown analytically to scale with the central, collapsed (virial) mass of the cluster.

The velocity dispersion of the galaxies around the cluster can also be used as an information carrier, since it correlates with the enclosed mass. However, the small number of halos which are large enough to be observed within some “neighboring” region around a single cluster is not adequate for an accurate calculation of the velocity dispersion. Here, we counteracted this effect by using “stacked” images combining several projections. The velocity dispersion of the halos around a cluster holds important promise for analyses of this type, and it is worth exploring further in future work.

As expected, contamination from distant halos that results from the use of photometric redshifts is affecting the results. Spectroscopic observations would generally result to a more accurate prediction of the turnaround radius.

All of the models, when tested on data that were acquired from different redshifts and different cosmologies were not successful in their predictions. For the models trained with the mass information this is expected since the turnaround radius scales with the mass for a specific redshift and cosmology. For the velocity trained models the same pattern appears, and our attempts for a straightforward rescaling that would allow the model to generalize were not successful, although they did improve performance somewhat (see appendix E.2), so this approach with different rescaling techniques might in fact hold the most promise for a machine-learning approach to identify the turnaround scale in a cosmology-independent way.

Future investigations could benefit from larger and higher-resolution datasets for training, with or without stacking. A proper Bayesian treatment or bias-reduction techniques such as the one described in Lin et al. (2022) could become particularly useful. Furthermore, more complex models e.g. with the use of inception layers in the architecture of the neural network, possibly combined with another kernel choice in smoothing the density field, or the use of Graph Neural Networks (GNNs) might be able to reveal additional information encoded in the mass and velocity information of galaxy clusters.

Acknowledgements. The CosmoSim database used in this paper is a service by the Leibniz-Institute for Astrophysics Potsdam (AIP). The MultiDark database was developed in cooperation with the Spanish MultiDark Consolider Project CSD2009-00064. The authors gratefully acknowledge the Gauss Centre for Supercomputing e.V. (www.gauss-centre.eu) and the Partnership for Advanced Supercomputing in Europe (PRACE, www.prace-ri.eu) for funding the MultiDark simulation project by providing computing time on the GCS Supercomputer SuperMUC at Leibniz Supercomputing Centre (LRZ, www.lrz.de). The Bolshoi simulations have been performed within the Bolshoi project of the University of California High-Performance AstroComputing Center (UC-HiPACC) and were run at the NASA Ames Research Center. The rest of the simulations in this paper were carried out by the Virgo Supercomputing Consortium using computers based at Computing Centre of the Max-Planck Society in Garching and at the Edinburgh Parallel Computing Centre. The data are publicly available at www.mpa-garching.mpg.de/galform/virgo/int_sims

References

Adhikari, S. & Huterer, D. 2019, *J. Cosmology Astropart. Phys.*, 2019, 036
 Baron, D. 2019, arXiv e-prints, arXiv:1904.07248
 Bernal, J. L., Verde, L., & Riess, A. G. 2016, *J. Cosmology Astropart. Phys.*, 2016, 019
 Carleo, G., Cirac, I., Cranmer, K., et al. 2019, *Reviews of Modern Physics*, 91, 045002
 Chen, T. & Guestrin, C. 2016, arXiv e-prints, arXiv:1603.02754
 Di Valentino, E., Melchiorri, A., & Silk, J. 2020, *Nature Astronomy*, 4, 196
 Di Valentino, E., Melchiorri, A., & Silk, J. 2021, *ApJ*, 908, L9
 Frenk, C. S., Colberg, J. M., Couchman, H. M. P., et al. 2000, arXiv e-prints, astro

Handley, W. 2021, *Phys. Rev. D*, 103, L041301
 Hildebrandt, H., Viola, M., Heymans, C., et al. 2017, *MNRAS*, 465, 1454
 Hoffman, Y., Carlesi, E., Pomarède, D., et al. 2018, *Nature Astronomy*, 2, 680
 Huertas-Company, M. & Lanusse, F. 2023, *PASA*, 40, e001
 Jenkins, A., Frenk, C. S., Pearce, F. R., et al. 1998, *ApJ*, 499, 20
 Joudaki, S., Mead, A., Blake, C., et al. 2017, *MNRAS*, 471, 1259
 Kingma, D. P. & Ba, J. 2014, arXiv e-prints, arXiv:1412.6980
 Korkidis, G. & Pavlidou, V. 2024, *A&A*, 690, A71
 Korkidis, G., Pavlidou, V., & Tassis, K. 2023, *A&A*, 674, A87
 Korkidis, G., Pavlidou, V., Tassis, K., et al. 2020, *A&A*, 639, A122
 Lahav, O. 2023, arXiv e-prints, arXiv:2302.04324
 Lee, J. 2016, *ApJ*, 832, 123
 Lee, J. 2018, *ApJ*, 856, 57
 Lee, J., Kim, S., & Rey, S.-C. 2015, *ApJ*, 815, 43
 Lee, J. & Li, B. 2017, *ApJ*, 842, 2
 Lee, J. & Yepes, G. 2016, *ApJ*, 832, 185
 Lin, Q., Fouchez, D., Pasquet, J., et al. 2022, *A&A*, 662, A36
 Motloch, P. & Hu, W. 2018, *Phys. Rev. D*, 97, 103536
 Pavlidou, V., Korkidis, G., Tomaras, T. N., & Tanoglidis, D. 2020, *A&A*, 638, L8
 Pavlidou, V. & Tomaras, T. N. 2014, *J. Cosmology Astropart. Phys.*, 2014, 020
 Planck Collaboration, Ade, P. A. R., Aghanim, N., et al. 2014, *A&A*, 571, A16
 Planck Collaboration, Aghanim, N., Akrami, Y., et al. 2020, *A&A*, 641, A6
 Raveri, M. & Hu, W. 2019, *Phys. Rev. D*, 99, 043506
 Riebe, K., Partl, A. M., Enke, H., et al. 2013, *Astronomische Nachrichten*, 334, 691
 Riess, A. G., Casertano, S., Yuan, W., et al. 2018, *ApJ*, 855, 136
 Riess, A. G., Casertano, S., Yuan, W., Macri, L. M., & Scolnic, D. 2019, *ApJ*, 876, 85
 Shah, P., Lemos, P., & Lahav, O. 2021, *A&A Rev.*, 29, 9
 Tanoglidis, D., Pavlidou, V., & Tomaras, T. 2016, arXiv e-prints, arXiv:1601.03740
 Tanoglidis, D., Pavlidou, V., & Tomaras, T. N. 2015, *J. Cosmology Astropart. Phys.*, 2015, 060
 Thomas, P. A., Colberg, J. M., Couchman, H. M. P., et al. 1998, *MNRAS*, 296, 1061
 Zhao, G.-B., Raveri, M., Pogosian, L., et al. 2017, *Nature Astronomy*, 1, 627

Appendix A: Additional data values distributions

In Fig. A.1 we present the distributions of the R_{ta} values from each of the additional MDPL2 redshift snapshots (left panel) and from each of the non- Λ CDM Virgo simulations (right panel), created with the same methods mentioned in Sect. 2.1. As expected, the distributions, even though similar in terms of general form, span over different R_{ta} values. In particular, the location of peaks changes between different redshifts and different cosmologies, as a direct result of ρ_{ta} being sensitive to redshift and cosmological parameters. If a model that successfully predicts the R_{ta} on all of the different regimes was created, it would mean the existence of an independent way of constraining ρ_{ta} and therefore Ω_m and Ω_Λ .

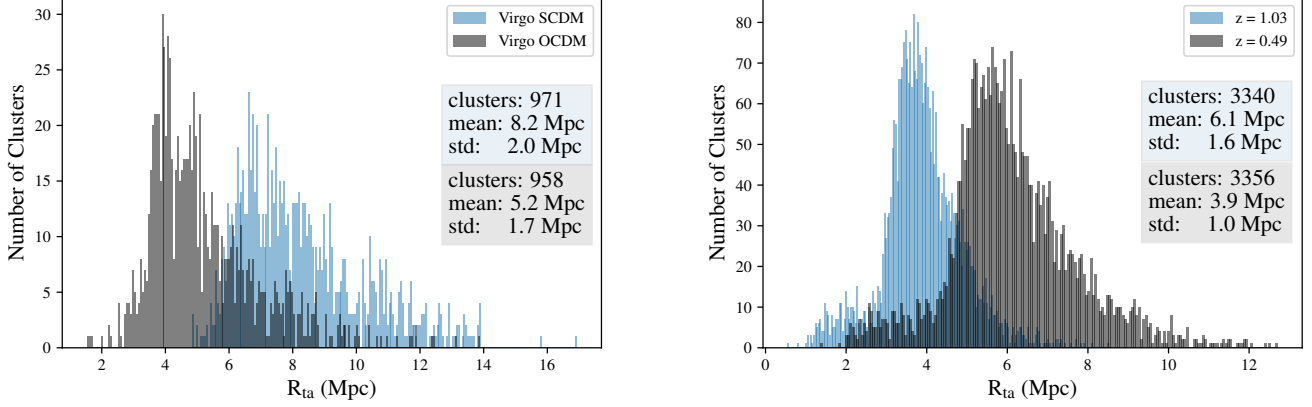


Fig. A.1. Histogram of R_{ta} values from MDPL2 form $z = 0.49$ and $z = 1.03$ (left panel) and Virgo from OCDM and Λ CDM cosmology (right panel), similarly to Fig.1. It is apparent that the distribution moves as we change the redshift or Ω_m and Ω_Λ , which is expected due to the dependence of ρ_{ta} on the cosmological setting discussed throughout the paper and proved in Pavlidou et al. (2020).

Appendix B: Architecture of the Neural Network

The NN architecture used can be seen in Table. B.1. During training, the Mean Absolute Error was used to evaluate the model's performance on the validation set. In addition to this basic architecture, the hyperparameters were tuned in each case to obtain the best result. In most of the cases the following additional elements were used: Activation function: ReLU, Padding: same, Kernel initializer: He initialization, Learning rate: 10^{-3} , optimizer: Adam (Kingma & Ba 2014). In some of the cases l1 and l2 regularizations were also implemented.

Table B.1. Characteristics of each layer of the CNN architecture. Columns are: name of the layer, input layer, size of the convolution kernel (in pixels), size (height \times width in pixels) and number of the resulting feature maps.

Layer	Inputs	Kernel size	$h \times w$	#feature maps
Convolution (C1)	Input image	5×5	25×25	32
Activation (A1)	C1	-	25×25	32
Batch Normalization (BN1)	A1	-	25×25	32
Pooling (P1)	BN1	2×2 (stride 1 pix)	12×12	32
Dropout (D1)	P1	-	12×12	32
Convolution (C2)	D1	5×5	25×25	64
Activation (A2)	C2	-	25×25	64
Batch Normalization (BN2)	A2	-	25×25	64
Pooling (P2)	BN2	2×2 (stride 1 pix)	12×12	64
Dropout (D2)	P2	-	12×12	64
Flatten (F1)	D2	-	2304	-
Fully Connected (FC1)	F1	-	32	-
Activation (A3)	FC1	-	32	-
Batch Normalization (BN3)	A3	-	32	-
Dropout (D3)	BN3	-	32	-
Fully Connected (FC2)	D3	-	16	-
Activation (A4)	FC2	-	16	-
Dropout (D4)	A4	-	16	-
Fully Connected (FC3)	D4	-	1	-

Appendix C: Velocity dispersion

In Fig. C.1 we demonstrate that acquiring R_{ta} from stacked velocity profiles is not straightforward. When computing the velocity dispersion images based on velocity data from 9 R_{ta} bins, the location of the turnaround scale is not identifiable “by eye” in the images.

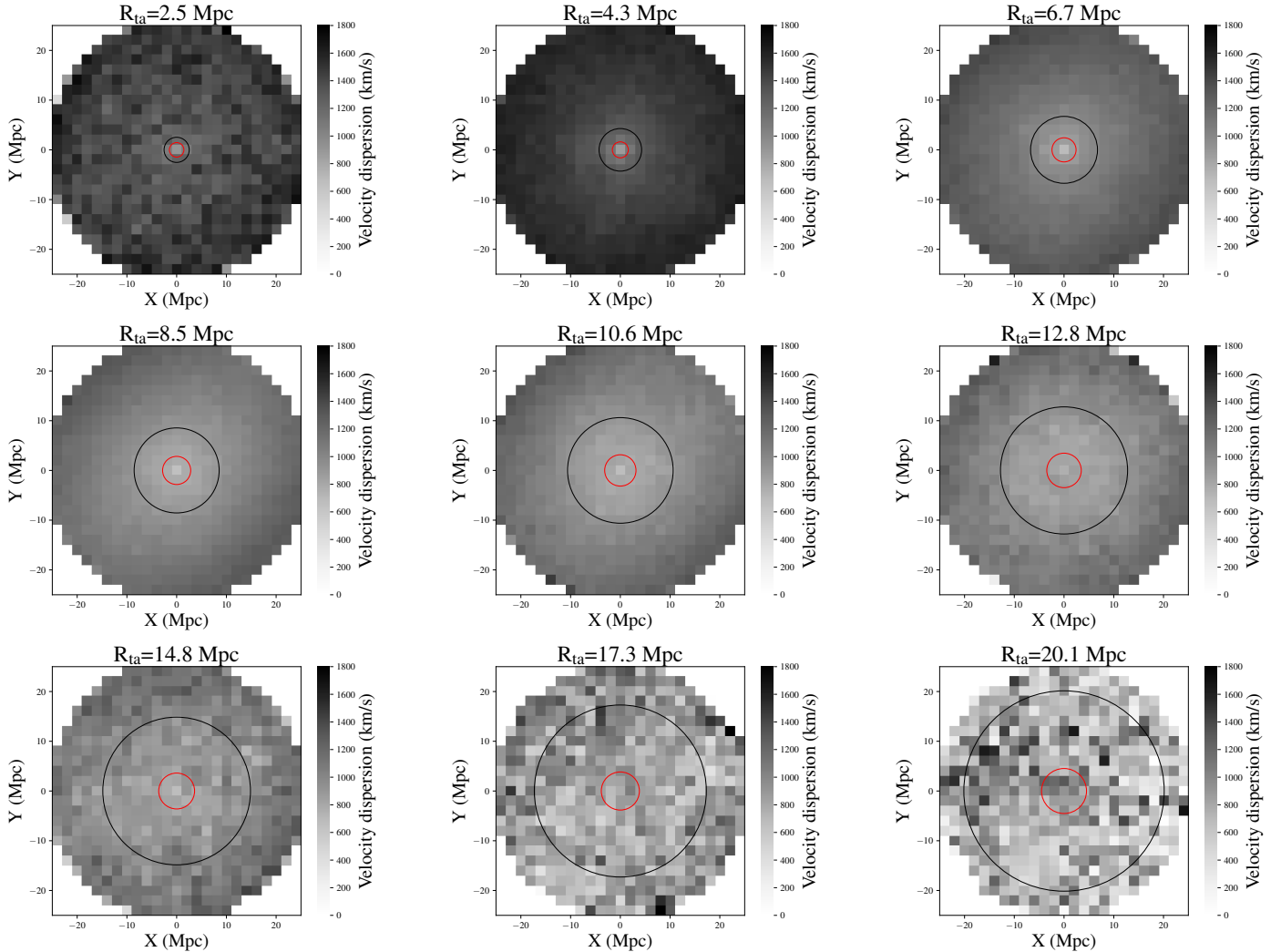


Fig. C.1. Stacked velocity dispersion images of the Merged MDPL2 and Virgo Λ CDM data. The turnaround values of the dataset have been segmented into 9 bins. All of the corresponding clusters’ projections of line-of-sight velocities, that belong in the same bin category, have been stacked on top of each other to create 9 images, calculating the standard deviation in each pixel. On the top of each image is the mean value of the turnaround radii in each bin which is represented with a black circle in each image. Red circles represent the mean R_{200} in each case. There is no apparent way of predicting the R_{ta} based on these images “by eye”, especially outside of the R_{ta} range 4.3 – 10.6 Mpc.

Appendix D: Stacked Velocity dispersion based on R_{200}

Here (Fig. D.1) we present the results that were computed in the same way as with Fig. 5 but this time with stacking of the images based on the R_{200} of the clusters. The results of the middle and right panels seem to demonstrate similar success while the left panel (only using MDPL2 data) seems to be better in this case. The reason behind this is probably due to better tracing of the global minimum during training.

Appendix E: CNNs vs “Classical” astrophysical approach

We have established that significant information about the turnaround radius is encoded in the velocity dispersion of galaxies in our mock observations, in the form the stacked images of our merged dataset (MDPL2 and Virgo Λ CDM). This was achieved by the somewhat unconventional use of 2D pixelized projections processed by CNNs. In the realm of astrophysics and cosmology, a more classical and commonly used approach would be to deduce information from the radial velocity profiles of the galaxy clusters. Here, we employ this method of more traditional compression, compare it with our previous results, and explore its limitations for generalizing to other redshifts.

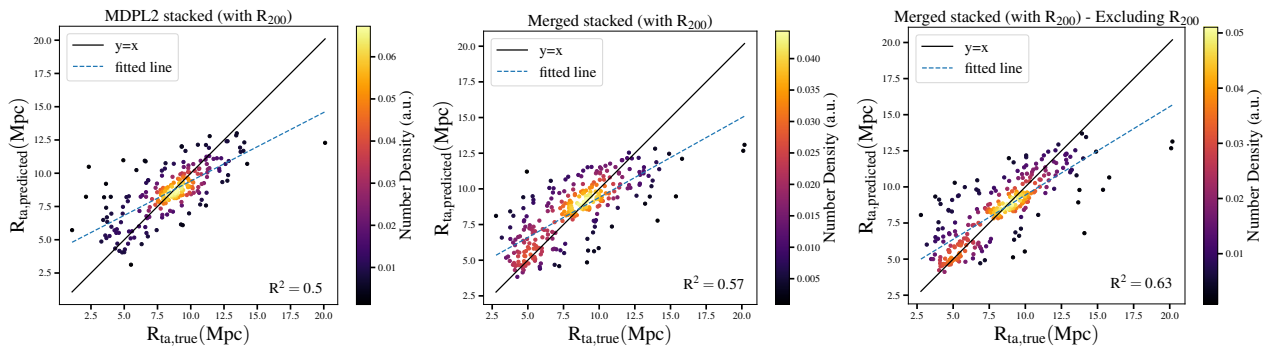


Fig. D.1. Comparison between predicted and true values of the R_{ta} for models using the "stacked" images from 3000 bins of R_{200} from: the MDPL2 data (*left panel*); the merged MDPL2 with Virgo Λ CDM data (*middle panel*); the merged MDPL2 with Virgo Λ CDM data with removed information inside the R_{200} of the central overdensity (*right panel*). R^2 scores are 0.5, 0.57 and 0.63 respectively. The colors represent the number density of the plotted points, calculated using a Gaussian kernel density estimate. It is apparent that the merging of the 2 datasets significantly improves the performance of the model even without the central halos' velocity information.

E.1. Baseline model

As our more traditional baseline we try to train a simple model, based on the mass and velocity radial profiles of the projections, with the XGBoost algorithm (Chen & Guestrin 2016). Here, instead of the 25×25 image creation described in Sect. 3.1 (2D array), we created a new dataset by calculating the mass column density and velocity dispersion in 25 radial bins in each projection (1D array). Consequently, each training instance has 25 features with the target variable being the turnaround radius.

Using the mass column density MDPL2 data, the model performs with the same success, having an R^2 score of 0.58 as seen in the left panel of Fig. E.1, where we plot the predicted vs true values in the same format as before. Again, this was an expected result since the model relies almost completely on the mass of the central cluster, which is not lost by the new type of compression.

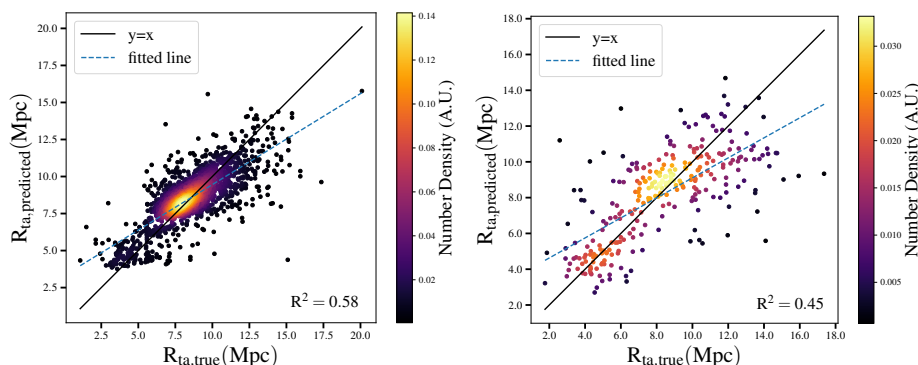


Fig. E.1. Comparison between predicted and true values of the R_{ta} for 1D models (features from radial bins only) using MDPL2 mass images (*left panel*) and the Merged MDPL2 and Virgo velocity dispersion images (*right panel*). The colors represent the number density of the plotted points, calculated using a Gaussian kernel density estimate.

A more interesting test is to compare the baseline model with the velocity dispersion data. After training it on the merged stacked dataset (which was previously the best candidate), testing resulted in an R^2 score of 0.45, as seen in the right panel of Fig. E.1. In this case, the original CNN outperforms this model (R^2 score: 0.57, middle panel of Fig. 5). The underlying reason of this behavior should be the more severe compression. This compression introduces a symmetry to our data which is not necessarily present in their original form. One important symmetry breaking component is the inclusion of structures outside of the 25 Mpc radius from the velocity cut, which the CNN seems to be able to discard. It should be noted that a merged dataset with 4 copies of each projection, each rotated by 90 degrees, was performing worse even with the use of the CNN, enhancing our previous argument.

E.2. Redshift normalization

At this point the superiority of the original CNN is already substantiated from the previous section. The only caveat is that our original model is not successful when tested on other cosmological settings. For this reason we make a final attempt to counter this issue for the velocity dispersion data. In particular, we try to normalize the velocity profiles in each redshift with the background universe, in order to let the model generalize.

Subsequently, we compute the mean value of the velocity dispersion of the last radial bin of all the projections of the training dataset in the same redshift. Then, we try 2 normalizations: dividing or subtracting the values of the bins with the mean value. We train the model with the MDPL2 and the Merged data on $z = 0$ and test on $z \approx 0.5$ and $z \approx 1.0$. The resulting R^2 scores can be seen in Table E.1.

Table E.1. R^2 scores of models trained on $z = 0$ and tested on $z \approx 0.5$ and 1.0 for the MDPL2 and the Merged data.

	Divide by outer ring	Subtract by outer ring
MDPL2		
$z = 0$	0.17	0.17
$z = 0.5$	-0.19	-0.36
$z = 1.0$	-7	-8
Merged		
$z = 0$	0.45	0.45
$z = 0.5$	0.22	0.17
$z = 1.0$	-2.18	-2.93

It can be seen that the model is not successful on other redshifts even with these normalizations, and again exhibits the same behavior of the lower R^2 score as we move away from the training redshift. However, the division of the outer ring in the merged dataset could suggest some potential for success, which requires further investigation beyond the scope of this work.